PORTLAND PRESS

Research Article

Engineering a monomeric variant of macrophage colony-stimulating factor (M-CSF) that antagonizes the c-FMS receptor

Yuval Zur[1],*, Lior Rosenfeld[1],*, Anna Bakhman[2], Stefan Ilic[3], Hezi Hayun[1], Anat Shahar[4], Barak Akabayov[3], Mickey Kosloff[2], Noam Levaot[5] and Niv Papo[1]

[1]Department of Biotechnology Engineering and the National Institute of Biotechnology in the Negev, Ben-Gurion University of the Negev, Beer-Sheva, Israel; [2]Department of Human Biology, Faculty of Natural Sciences, University of Haifa, Haifa, Israel; [3]Department of Chemistry, Ben-Gurion University of the Negev, Beer-Sheva, Israel; [4]The National Institute for Biotechnology in the Negev (NIBN), Beer-Sheva, Israel; and [5]Department of Physiology and Cell Biology, Ben-Gurion University of the Negev, Beer-Sheva, Israel

Correspondence: Mickey Kosloff (kosloff@sci.haifa.ac.il), Noam Levaot (levaot@bgu.ac.il) or Niv Papo (papo@bgu.ac.il)

Enhanced activation of the signaling pathways that mediate the differentiation of mononuclear monocytes into osteoclasts is an underlying cause of several bone diseases and bone metastasis. In particular, dysregulation and overexpression of macrophage colony-stimulating factor (M-CSF) and its c-FMS tyrosine kinase receptor, proteins that are essential for osteoclast differentiation, are known to promote bone metastasis and osteoporosis, making both the ligand and its receptor attractive targets for therapeutic intervention. With this aim in mind, our starting point was the previously held concept that the potential of the M-CSF$_{C31S}$ mutant as a therapeutic is derived from its inability to dimerize and hence to act as an agonist. The current study showed, however, that dimerization is not abolished in M-CSF$_{C31S}$ and that the protein retains agonistic activity toward osteoclasts. To design an M-CSF mutant with diminished dimerization capabilities, we solved the crystal structure of the M-CSF$_{C31S}$ dimer complex and used structure-based energy calculations to identify the residues responsible for its dimeric form. We then used that analysis to develop M-CSF$_{C31S,M27R}$, a ligand-based, high-affinity antagonist for c-FMS that retained its binding ability but prevented the ligand dimerization that leads to receptor dimerization and activation. The monomeric properties of M-CSF$_{C31S,M27R}$ were validated using dynamic light scattering and small-angle X-ray scattering analyses. It was shown that this mutant is a functional inhibitor of M-CSF-dependent c-FMS activation and osteoclast differentiation *in vitro*. Our study, therefore, provided insights into the sequence–structure–function relationships of the M-CSF/c-FMS interaction and of ligand/receptor tyrosine kinase interactions in general.

Introduction

Recombinant protein ligands and receptors have shown great promise as biotherapeutics [1,2], with more and more drugs of this type being approved for clinical use. Modified ligands or receptors with altered and potentially applicable therapeutic properties can be generated via rational design [3]. In some cases, the rational design of the attributes required for an effective therapeutic involves converting the activity of the ligand or receptor from agonistic to antagonistic. Several examples of the conversion of receptor tyrosine kinase (RTK) agonistic ligands to antagonists can be found in the literature, including the engineering of vascular endothelial growth factor [4], human growth hormone [5], and stem cell factor [6,7]. In all these cases, ligand dimerization, which is necessary for receptor activation, was targeted by converting the dimeric ligand to a monomer that antagonizes the receptor.

An important recent example for converting a ligand agonist into an antagonist is the engineering of receptor activator of nuclear factor κ B ligand (RANKL) to antagonize its receptor as a potential treatment for osteoporosis [8].

RANKL is involved in osteoporosis and bone metastasis development via its effect on the differentiation of monocytes to osteoclasts. To initiate this differentiation, the cells must be continuously exposed to macrophage colony-stimulating factor (M-CSF) [9,10]. The M-CSF ligand and its RTK, c-FMS, have thus generated great interest as potential therapeutic targets in bone diseases. In osteoporosis, intact M-CSF signaling is essential for the survival, proliferation, and differentiation of osteoclasts. In cancers, the M-CSF/c-FMS interaction has been shown to elevate the risk for bone metastasis in breast, lung, and prostate cancer [11–13] and to enhance the growth of several cancer types [14–17].

M-CSF has two functional interfaces for protein–protein interaction. The first, which contains a cysteine in position 31, mediates M-CSF dimerization. A Cys31–Cys31 disulfide bond across the homodimer interface covalently links — and hence stabilizes — the M-CSF dimer [18]. The other interface is that with the c-FMS receptor — binding of the M-CSF dimer to c-FMS leads to receptor dimerization, autophosphorylation, and activation [19–21]. Receptor activation then stimulates the downstream signaling pathways, which include PI3K, Src, Grb2, and c-Cbl; these, in turn, mediate osteoclast and macrophage proliferation, differentiation, and survival [22,23]. While these pathways have been studied mostly using monoclonal antibodies or small molecule kinase inhibitors, details of the exact relationship between M-CSF dimerization and c-FMS receptor autophosphorylation and activation of downstream cellular targets are still lacking. Therefore, the development of M-CSF-derived c-FMS antagonists will provide: (1) tools for elucidating the molecular mechanisms that mediate M-CSF-induced c-FMS activation and osteoclast differentiation and (2) non-immunoglobulin-based therapeutics that will specifically target the c-FMS receptor for the treatment and disease management of osteoporosis and various types of cancer.

The concept of converting the M-CSF ligand into a monomer (M-CSF$_{C31S}$) was first explored by the Rettenmier group using site-directed mutagenesis [24]. In a recent biochemical study, we showed that this variant does not dimerize in concentrations of up to 500 nM [19]. In both these studies [19,24], M-CSF$_{C31S}$ was not tested for functional antagonistic activity in the presence of M-CSF$_{WT}$ — neither with murine macrophages nor with human monocytes.

In contrast with the above studies, here we show that M-CSF$_{C31S}$ is able to form non-covalently linked dimers, and that it, therefore, retains significant agonistic activity — limiting its potential as a therapeutic. As a first step in our efforts to convert the agonistic activity into antagonistic, we solved the crystal structure of the M-CSF$_{C31S}$ dimer complex, thereby revealing the molecular basis for the non-covalent dimerization of M-CSF$_{C31S}$. We analyzed this structure using an energy-based approach and subsequently re-designed a monomeric M-CSF variant, M-CSF$_{C31S,M27R}$. We then used experimental biophysical and biological testing to show that this re-designed protein is a highly potent M-CSF antagonist and a potent inhibitor of c-FMS signaling and osteoclast differentiation *in vitro*. Our findings suggest that M-CSF$_{C31S,M27R}$ may serve as a potent therapeutic agent for the above-mentioned c-FMS-related diseases. More generally, our study suggests that potent inhibitors for other RTKs can be generated by a similar structure-based approach, which would also facilitate further investigation of the mechanisms underlying activation of RTKs. Moreover, our results reveal that when using this approach, care needs to be taken when designing other potential ligand-based inhibitors for other RTKs, and only when ligand dimerization is completely abolished does inhibition occur as designed.

Materials and methods
Crystallization and structure determination
M-CSF$_{C31S}$ was concentrated to 5.5 mg/ml. Initial crystallization-condition screening was performed using an Index screening kit (Hampton Research) at 293 K. Each drop contained a mixture of 0.3 μl of crystallization solution and 0.3 μl of M-CSF$_{C31S}$ protein solution. Crystals grew for 9 days and were harvested from a drop containing the following optimized crystallization solution: 0.03 M bis–Tris (pH 6.5); 0.17 M Mg-formate; 16.67% PEG 3350; and 0.07 M bis–Tris (pH 5.5). The crystals were flash-cooled in liquid nitrogen prior to data collection. A diffraction dataset was collected on beamline BM14 at the European Synchrotron Radiation Facility (ESRF, Grenoble, France) to a maximum resolution of 2 Å. Data were measured at 0.979 Å for 250 images with an oscillation range of 1°, an exposure time of 3 s per image, and a crystal-to-detector distance of 181.45 mm. Data processing was performed using the HKL2000 program suite [25]. Phase acquisitions and

structure determination were performed using Phaser [26] of the CCP4 Program Suite [27]. The final model was built by Coot [28] and refined using Phenix [29].

Energy calculations to identify the M-CSF$_{C31S}$ residues that contribute significantly to dimer formation

We followed the methodology described previously [30] to analyze the per-residue contributions of the M-CSF$_{C31S}$ residues to dimer formation. The finite difference Poisson–Boltzmann (FDPB) method was used to calculate the net electrostatic and polar contributions ($\Delta\Delta G_{elec}$) of each residue that is within 15 Å of the dimer interface. Non-polar energy contributions ($\Delta\Delta G_{np}$) were calculated as a surface-area proportional term, by multiplying the per-residue surface area buried upon complex formation (calculated using surfv [31]) by a surface tension constant of 0.05 kcal/mol/Å^2 [32]. Energetically significant residues were defined as those contributing $\Delta\Delta G_{elec}$ or $\Delta\Delta G_{np} > 1$ kcal/mol to the interactions.

Protein expression and purification

The three computationally selected M-CSF variants, namely, M-CSF$_{C31S,Q26R}$, M-CSF$_{C31S,M27R}$, and M-CSF$_{C31S,Q26R,M27R}$, as well as M-CSF$_{C31S}$ and M-CSF$_{WT}$, were purified using the GS115 *Pichia pastoris* yeast strain, as recently described [19]. M-CSF$_{C31S}$ and M-CSF$_{WT}$ were purified using a Superdex 200 16/600 column (GE Healthcare), whereas M-CSF$_{C31S,M27R}$, M-CSF$_{C31S,Q26R}$, and M-CSF$_{C31S,Q26R,M27R}$ were purified using a Superdex 75 10/300 column (GE Healthcare).

BS^3 cross-linking assay

Human (4 μg) and murine M-CSF$_{WT}$ (1 μg), M-CSF$_{C31S}$ (1 μg), and M-CSF$_{C31S,M27R}$ (2.5 μg) were incubated with different concentrations of BS^3 [bis(sulfosuccinimidyl)suberate] (ThermoFisher Scientific, MA, U.S.A.) cross-linker (0, 25, 100, 250, 500, 1000, and 2500 μM) for 30 min at room temperature. Then, bis–Tris buffer was added to a final concentration of 30 mM, and the mixture was incubated for 15 min at room temperature. Samples were denatured with sample buffer, boiled, and loaded on 15% SDS–PAGE for protein separation. The gels were stained with InstantBlue staining (Expedeon, CA, U.S.A.) for 40 min, followed by two washing steps with double distilled water. The gels were visualized with MiniBis pro (DNR Bio-Imaging Systems, Jerusalem, Israel).

Dynamic light scattering

The hydrodynamic radii of M-CSF$_{WT}$, M-CSF$_{C31S}$, and M-CSF$_{C31S,M27R}$ were determined using dynamic light scattering (DLS). The proteins, in a concentration of 0.5 mg/ml, were filtered to remove aggregates and contaminants. Light scattering was measured at an angle of 90° three times, in two different experiments, resulting in a total of six measurements. Another measurement was performed at an angle of 60° to verify that the radius did not change with the measurement angle. An analysis of the solution was conducted to verify that the most abundant species were in the size range of 1–10 nm. The peak for these species was compared for the three different proteins, and the hydrodynamic radius of each was determined as the maximum of the peak.

Small-angle X-ray scattering analysis

Small-angle X-ray scattering (SAXS) data were collected on the SAXLAB GANESHA 300 XL system, possessing a Genix 3D Cu-source with an integrated monochromator, three pinholes collimation, and a two-dimensional Pilatus 300K detector. The scattering intensity was recorded in the interval of $0.012 < q < 0.7$ Å^{-1}. The measurements were performed under vacuum at 25°C. All three M-CSF variants were measured at concentrations of 3, 5, and 7 mg/ml. The scattering of the buffer was also measured and subtracted from the scattering of the samples.

The magnitude of the scattering vector is described by the following equation:

$$q = \frac{4\pi\sin\theta}{\lambda}$$

where 2θ is the scattering angle and λ is the wavelength.

Values for the radius of gyration (R_g) were derived from the small-angle part of the SAXS profile (Guinier region, $qR_g < 1.0$), in PRIMUS [33]. In this region, Guinier approximation is applicable:

$$I(q) = I(0)e^{((-R_g^2 q^2)/3)}$$

R_g values were also derived using in-house scripts [34] designed to perform an automatic search for the best-fitting parameters using GNOM [35]. CRYSOL [36] was used to compute the theoretical SAXS spectra based on the M-CSF$_{WT}$ crystal structure (PDB ID code: 3UF2). These spectra served as a reference for reconstruction of the experimental SAXS data. GASBOR [37] was used to reconstruct the molecular envelope based on the best GNOM fit obtained from the in-house script. Ten models were calculated for each sample and averaged using DAMAVER [38].

Surface plasmon resonance

The ability of M-CSF$_{WT}$ and M-CSF$_{C31S,M27R}$ to bind the c-FMS receptor was determined by surface plasmon resonance (SPR) spectroscopy on a ProteOn XPR36 (Bio-Rad, CA, U.S.A.). M-CSF variants were immobilized on the surface of the chip using the amine coupling reagents, sulfo-NHS (0.1 M N-hydroxysuccinimide) and EDC (0.4 M 1-ethyl-3-(3-dimethylaminopropyl)-carbodiimide). For chip activation, followed by 1 μg of the proteins in 10 mM sodium acetate buffer (pH 4.0), to give 1063 and 551 response units (RU) for M-CSF$_{WT}$ and M-CSF$_{C31S,M27R}$, respectively. BSA (3 μg; 3762 RU) was immobilized on the chip as a negative control. Unbound esters were deactivated with 1 M ethanolamine HCl at pH 8.5. Before each binding assay, the temperature was set at 25°C. Soluble human c-FMS receptor (extracellular domains, residues Met1–Glu512) (Sino Biological, China) was then allowed to flow over the surface-bound M-CSF, at concentrations of 4.375, 8.75, 17.5, 35, and 70 nM and a flow rate of 25 μl/min for 16 min 21 s, and during this time, the interactions between M-CSF and c-FMS were measured. The dissociation of the proteins was measured, while allowing PBST (phosphate-buffered saline + 0.005% Tween) to flow over the surface for 6 min and 50 s at a flow rate of 50 μl/min. This process was repeated three times, with a regeneration step between runs. The regeneration was conducted with 50 mM NaOH at a flow rate of 100 μl/min. For each protein complex, a sensorgram was generated from the RUs measured during the course of the protein–protein interaction minus the values of the BSA channel. The dissociation constant (K_D) was determined from the sensorgram of the equilibrium-binding phase.

Phosphorylation assay

The experiment was performed on two cell types, bone marrow-derived monocytes (BMMs) and human peripheral blood CD14$^+$ monocytes, as follows: (i) BMMs from wild-type C57BL6 mice were purified by flushing the bone marrow from the femur and tibia, as previously described [39]. The cells were treated with ACK red cells lysis buffer (ThermoFisher Scientific, U.S.A.) and grown in complete α-MEM growth medium (Sigma–Aldrich, U.S.A.) containing 10% fetal bovine serum (FBS) (selected to not contain LPS to prevent macrophage differentiation), penicillin, streptomycin, and L-glutamine. Recombinant murine M-CSF was added at a concentration of 40 ng/ml (Peprotech, Israel) for 3 days at 37°C to induce adhesion and proliferation of monocytes. Then, 7×10^5 cells were transferred into a six-well plate with complete α-MEM and 20 ng/ml murine M-CSF and RANKL (R&D Systems, U.S.A.) for 48 h. (ii) CD14$^+$ monocytes (Lonza, Switzerland) were grown in complete α-MEM for 5 days in the presence of human M-CSF (20 ng/ml). Then, 3.5×10^5 cells were transferred to a 24-well plate with a complete α-MEM, 20 ng/μl human M-CSF (R&D Systems, U.S.A.) and 20 ng/ml murine RANKL for 72 h. At this point, the medium was replaced with a starvation medium (α-MEM without FBS) for 4 h. After starvation, the cells were washed with PBS and incubated in a starvation medium containing 0.5 nM murine (BMMs) or human (CD14$^+$) M-CSF and 100 nM (CD14$^+$ cells) or 1 μM (BMMs) of either M-CSF$_{C31S}$ or M-CSF$_{C31S,M27R}$ for 1 min. To test the phosphorylation levels in the absence of murine M-CSF$_{WT}$, we incubated 0.5, 5, 10, 50, 1000, and 5000 nM of M-CSF$_{C31S}$ or M-CSF$_{C31S,M27R}$ and 0.5, 5, and 10 nM of human M-CSF$_{WT}$ with the cells. The positive control contained 0.5 nM murine (BMMs) or human (CD14$^+$) M-CSF, and the negative control was incubated in starvation medium without any added protein. The cells were transferred to ice, and lysis buffer [deoxycholate 0.5%, 25 nM NaF, 10 mM NaPO$_4$, 1 mM sodium orthovanadate, 5 mM EDTA (pH 7.4), 5 mM EGTA (pH 7.4), 100 mM NaCl, 2% Triton X-100] was added. The cells were detached, collected, incubated on ice for 10 min, and centrifuged at 14 000 ***g*** for 30 min, and the supernatants

were transferred to a fresh tube. Western blot was performed on all samples, with anti-c-FMS, anti-phosphorylated c-FMS, or anti-β-actin antibody produced in rabbit as a primary antibody (Cell Signaling Technologies, MA, U.S.A.). A secondary HRP-linked anti rabbit antibody was then added, and the signal was developed using the EZ-ECL kit (Biological Industries, Israel). The chemiluminescent signal was imaged with Fusion FX (Vilber Lourmat, Germany). The images were quantified using ImageJ [40]. The quantified intensity values of the phosphorylated c-FMS for each sample were divided by the total c-FMS intensity and then by the β-actin expression intensity. The value of the positive control was set as 1, and other samples were normalized according to it.

Differentiation assay

BMMs and CD14$^+$ cells were obtained and grown as described above. The plates containing the monocytes were washed with PBS; the cells were detached using a cell scraper for BMMs or Accutase (Biological Industries, Israel) for CD14$^+$; and 2×10^4 BMMs or 1×10^4 CD14$^+$ cells were transferred to each well in a 96-well plate. Osteoclast differentiation was induced as described in the 'Phosphorylation Assay' section. To determine the influence of M-CSF$_{C31S}$ and the M-CSF$_{C31S,M27R}$ on osteoclast differentiation, the proteins were added to the differentiation medium (with M-CSF and RANKL) in different concentrations (50 nM, 1 μM, and 5 μM for BMMs and 50 nM, 250 nM, and 1 μM for CD14$^+$). BMM and CD14$^+$ cells were treated with different inhibitor concentrations, because BMMs express murine c-FMS with 10-fold lower affinity toward human M-CSF when compared with CD14$^+$ cells. To determine the influence of human M-CSF$_{WT}$ on the differentiation, it was added to the cells in different concentrations (50 nM, 1 μM, and 5 μM) without adding murine M-CSF$_{WT}$. Once the cells were fully differentiated, they were fixed with 4% paraformaldehyde and stained using the tartrate-resistant acid phosphatase (TRAP) staining kit (Sigma–Aldrich, U.S.A.) according to the manufacturer's protocol. As the positive control, cells were incubated with M-CSF and RANKL without inhibitors, and the negative control was composed of cells that were incubated in a differentiation medium without RANKL. Osteoclast parameters were obtained by the analysis of 20 images from random areas in each well; the osteoclasts were observed with an Olympus 83× microscope with an automated stage. Cells in each image were counted in a double-blind manner, and the number of nuclei in the osteoclasts was determined using the ImageJ software. For the positive control of BMMs, an average of 28.33 osteoclasts and 135 nuclei per well were counted. For CD14$^+$ positive control, the average numbers of osteoclasts and nuclei were 14.5 and 75, respectively, per well. The results for each parameter were normalized to the positive control values.

Statistical analysis

The data from the c-FMS phosphorylation assay and cell differentiation assays were analyzed for column statistics with GraphPad Prism, version 5.00, for Windows (La Jolla, CA, U.S.A.). Data are shown as means ± SEM or means ± SD. Statistical significance was determined by column statistics and t-test analysis. A P-value of <0.05 was considered statistically significant.

Results

Crystallization of M-CSF$_{C31S}$ and computational analysis of residues contributing to dimer formation

To generate a monomeric M-CSF variant, we first crystallized the M-CSF$_{C31S}$ variant, which cannot form an intramolecular disulfide bond at position 31. Purified M-CSF$_{C31S}$ was subjected to several crystallization trials using the sitting drop vapor diffusion method, and crystals were formed after 9 days. The data set used for structure determination was collected at BM14 beamline at the ESRF (Grenoble, France). The crystal structure was solved to a maximum resolution of 2.0 Å (Figure 1A, PDB ID: 5LXF) by molecular replacement, using as a search model PDB ID: 3UF2. A summary of the diffraction data collection statistics is given in Supplementary Table S1.

Surprisingly, M-CSF$_{C31S}$ showed only minor tertiary structural differences relative to wild-type M-CSF (M-CSF$_{WT}$) and essentially no differences in the quaternary dimeric structure (Figure 1). In the same location of the C31–C31 disulfide bond in the M-CSF wild type (Figure 1B), we observed a S31–S31 hydrogen bond between the serine side chains (Figure 1D). The M-CSF$_{WT}$ and M-CSF$_{C31S}$ mutant structures superimposed with a root-mean-square deviation (RMSD) of the backbone atom positions of ~1 Å over the full length of the structures, and were very similar across the entire chain (Figure 1C). The dimer interface of the mutant was
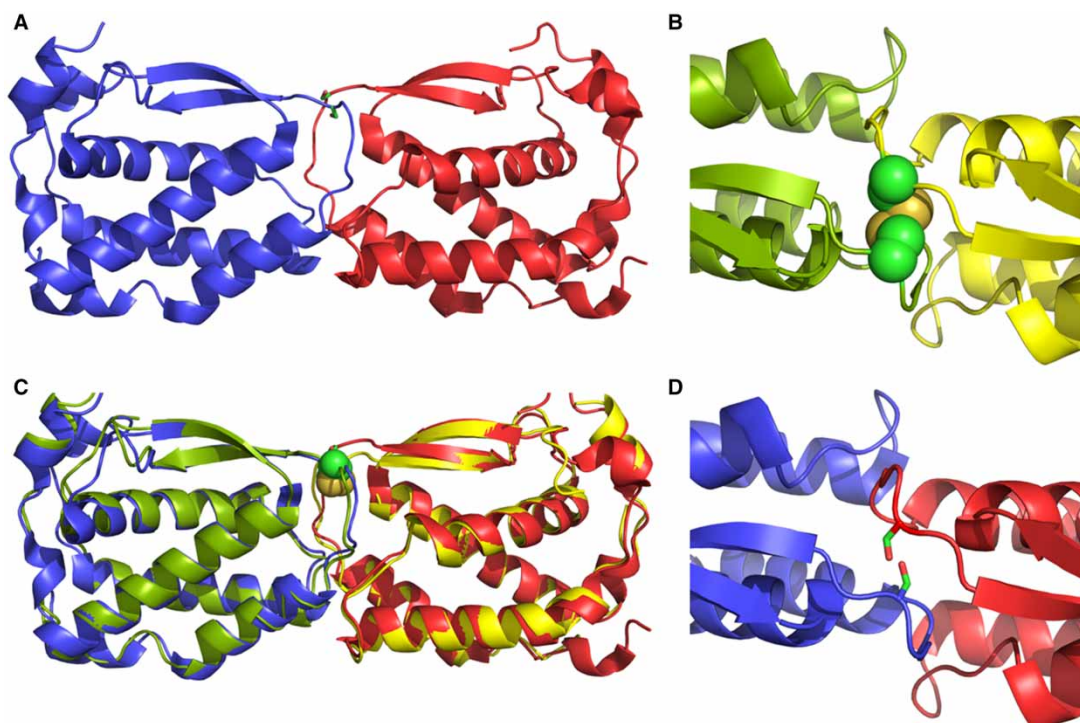
Figure 1. Structure of the M-CSF$_{C31S}$ mutant, compared with the M-CSF wild-type structure.
(**A**) X-ray structure of the dimeric M-CSF$_{C31S}$ mutant solved here, shown in ribbon diagram with S31 visualized as sticks.
(**B**) Close-up of the C31–C31 disulfide bond in the wild-type M-CSF structure (PDB ID 3UF2), visualized as spheres and
colored by atom. The structure is rotated 90° about X in relation to the M-CSF$_{C31S}$ mutant shown in **A**. (**C**) Overlay of the
M-CSF$_{C31S}$ mutant structure on the M-CSF wild-type structure, with the two C31 residues from the latter shown as spheres.
(**D**) Close-up of the S31 residues in the M-CSF$_{C31S}$ mutant dimer, visualized as in **B**.

highly similar to that of the wild type, suggesting that the M-CSF$_{C31S}$ mutation is not sufficient to prevent the
formation of an M-CSF dimer and that further mutagenesis is required to abolish dimerization.

We, therefore, used an energy-based approach to identify critical positions as candidates for mutagenesis
to perturb the dimer interface. Using the M-CSF$_{C31S}$ dimeric structure as input, we applied energy calculations
to identify the residues that contribute significantly to the M-CSF$_{C31S}$–M-CSF$_{C31S}$ dimer interface, according to
the methodology we developed previously [30]. We used the FDPB method to calculate the net electrostatic
and polar contributions ($\Delta\Delta G_{elec}$) of each M-CSF$_{C31S}$ residue that is within 15 Å of the dimer interface.
Non-polar energetic contributions ($\Delta\Delta G_{np}$) were calculated as a surface-area proportional term by multiplying
the per-residue surface area buried upon complex formation by a surface tension constant of 0.05 kcal/mol/Å^2.
We defined energetically significant residues as those contributing $\Delta\Delta G_{elec}$ or $\Delta\Delta G_{np} \geq 1$ kcal/mol to the
interactions.

This approach identified 12 interfacial M-CSF$_{C31S}$ residues that made significant contributions to the inter-
molecular interactions between the two M-CSF molecules (Table 1, Figure 2A,B, and Supplementary
Figure S1). These residues reside in two segments of M-CSF. The main segment includes most of the residues
between D24–I33 (Figure 2A). The second shorter segment includes a hydrophobic residue (F67) and three
charged/polar residues — R66, R68, and N73 (Figure 2B).

After comparing the M-CSF$_{C31S}$ structure with the structure of the complex of murine M-CSF$_{WT}$ with the
c-FMS receptor (PDB ID: 3EJJ) [41], we identified only two M-CSF residues, Q26 and M27, that fulfilled the
following four conditions: (1) especially strong contributions to dimer formation, (2) lack of involvement in
receptor binding, (3) minimal intramolecular interactions that could affect monomer stability, and (4) a pre-
dicted introduction of strong steric interference between the two M-CSF monomers upon mutation. Of the 12
residues we identified, the four residues in the shorter segment (R66, F67, R68, and N73) were adjacent to
c-FMS and therefore could affect receptor binding. The mutated S31 residue resides at the periphery of the

Table 1 Per-residue energy contributions to interaction across the M-CSF dimer interface, calculated as described in Materials and Methods

M-CSF residue	Energy contribution to M-CSF dimer formation	Residue adjacent to c-FMS
D24	sc + mc + np	
S25	np	
Q26	sc + np (symmetry contact with corresponding Q26 across the dimer interface)	
M27	np (~150 Å² buried in adjacent monomer, no intramolecular interactions)	
E28	np	
T29	np	
S31	np + sc	
I33	np	
R66	mc + np	+
F67	np	+
R68	sc + mc + np	+
N73	mc + np	+

Abbreviations: np, non-polar; sc, side-chain electrostatic contribution; mc, main chain electrostatic contribution.

dimer interface and made only a small electrostatic contribution via a hydrogen bond with the S31 residue across the dimer interface. It was, therefore, not deemed a critical contributor to dimer formation in the M-CSF$_{C31S}$ mutant and being in the interface periphery — less likely to perturb interactions upon further mutations. D24, while making strong electrostatic and non-polar contributions, is also at the periphery of the dimer interface, and interacts with R68, and therefore might also affect receptor binding. Finally, the rest of the residues made only moderate non-polar contributions, were more peripheral, and therefore were not deemed critical for dimer formation.

On the other hand, our energy-based analysis showed that Q26 interacts symmetrically with the corresponding Q26 from the partner M-CSF$_{C31S}$ monomer via both side-chain to side-chain hydrogen bonds and non-polar contributions (Figure 2C), and that this residue also forms a hydrogen bond with S31 across the
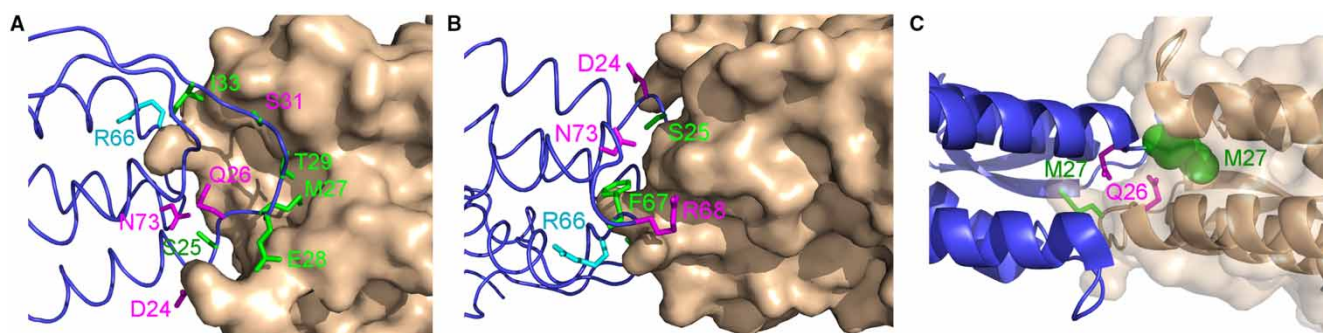

Figure 2. M-CSF$_{C31S}$ residues calculated to contribute significantly to the interaction across the M-CSF$_{C31S}$ dimer interface.
(**A**) M-CSF$_{C31S}$ residues calculated to contribute significantly to interactions across the dimer interface (see Table 1 and Supplementary Figure S1), shown as sticks and colored by the type of their energy contribution as follows: magenta (polar/electrostatic contribution from the side-chain + a non-polar contribution), cyan (polar/electrostatic contribution from the main chain + a non-polar contribution), and green (non-polar contribution only). The opposing monomer is shown as surface representation colored wheat. (**B**) As in **A**, rotated 180° about X. (**C**) Orientation of Q26 and M27, which contribute significantly and were deemed to be particularly influential on dimer formation and therefore chosen for further mutagenesis, shown as sticks (Q26 from both monomers and one of the M27 residues) and spheres (the M27 residue from the opposing monomer).

dimer interface (not shown). Thus, we hypothesized that mutating this residue to arginine would introduce both electrostatic repulsion (due to the symmetry-based intermolecular interaction of this residue) and steric hindrance to dimer formation due to the larger size of arginine.

The second critical residue, M27, which is not involved in any intramolecular interaction, extends deep into the opposing M-CSF$_{C31S}$ monomer (Figure 2C). As a result, ~150 Å^2 of surface area is buried within the opposing monomer due to each M27, more than any other M-CSF$_{C31S}$ residue (Supplementary Figure S1). We chose to mutate this residue to arginine as well, with the aim to introduce both a steric hindrance and a positive charge into a hydrophobic environment.

We then evaluated experimentally three different mutants designed on the basis of M-CSF$_{C31S}$, namely, M-CSF$_{C31S,Q26R}$, M-CSF$_{C31S,M27R}$, and a combination of the two mutations, M-CSF$_{C31S,Q26R,M27R}$. The three variants, as well as M-CSF$_{WT}$ and M-CSF$_{C31S}$, were purified using the *P. pastoris* GS115 yeast strain (Supplementary Figure S2). M-CSF$_{C31S,Q26R}$ and M-CSF$_{C31S,Q26R,M27R}$ were found to be extremely unstable in solution, i.e. aggregated and precipitated very rapidly, and we therefore focused on M-CSF$_{C31S,M27R}$.

Analysis of the dimerization of M-CSF$_{WT}$, M-CSF$_{C31S}$, and M-CSF$_{C31S,M27R}$

To validate our structural and computational analysis and to verify that M-CSF$_{C31S,M27R}$ is indeed a monomer, several biophysical assays were conducted. First, purified murine and human M-CSF$_{WT}$, M-CSF$_{C31S}$, and M-CSF$_{C31S,M27R}$ were cross-linked via lysine residues using different amounts of BS^3 reagent, and the proteins sizes were evaluated using SDS–PAGE (Figure 3A). Murine M-CSF$_{WT}$ served as positive control because it has a lysine in the dimerization site (K68), which facilitates the intermolecular cross-linking of the two monomers in the dimer. Indeed, murine M-CSF$_{WT}$ was observed almost entirely in a band with a molecular mass that fits the dimer size (~40 kDa) upon the addition of the cross-linker. In contrast, human M-CSF$_{WT}$, which has an arginine in the same position, produced only a faint band in a size that corresponds to a dimer, even at high concentrations of BS^3. M-CSF$_{C31S}$ gave a mixture of monomer and dimer bands (~20 and ~40 kDa). The dimer band became more prominent at higher BS^3 concentrations. It is likely that the non-covalent dimerization allows other lysines in M-CSF$_{C31S}$ to come into close proximity and cross-link. Importantly, M-CSF$_{C31S,M27R}$ did not produce any band corresponding to a dimer, even at high BS^3 concentrations. These results are in agreement with the structure-based computational redesign.

Next, the size of the M-CSF variants was evaluated in solution. M-CSF$_{WT}$, M-CSF$_{C31S}$, and M-CSF$_{C31S,M27R}$ at concentrations of 0.5 mg/ml were subjected to DLS analysis at an angle of 90°. The peaks for the most abundant species in each sample were compared (Figure 3B), and an estimated hydrodynamic radius was calculated from each peak. The hydrodynamic radii were found to be 3.73 ± 0.19, 3.56 ± 0.24, and 2.94 ± 0.10 nm for M-CSF$_{WT}$, M-CSF$_{C31S}$, and M-CSF$_{C31S,M27R}$, respectively. Since the proteins are not completely globular, the calculated radii do not represent the actual size of the molecules, but they do enable comparing the sizes of the proteins. M-CSF$_{C31S,M27R}$ was indeed found to be significantly smaller than the other two variants, supporting the hypothesis that the former is a monomer. To confirm that the oligomeric state of M-CSF$_{C31S,M27R}$ is not concentration-dependent, all M-CSF variants were subjected to SAXS measurements at concentrations of 3, 5, and 7 mg/ml. The radii of gyration (R_g) determined from SAXS data are presented in Figure 3C. We note that the R_g values remained within a similar range for M-CSF$_{WT}$ and M-CSF$_{C31S}$. There was a slight increase in the R_g value of M-CSF$_{C31S,M27R}$ at higher concentrations, presumably due to an increase in interparticle interactions. Still, the R_g value at the lowest M-CSF$_{C31S,M27R}$ concentration was significantly lower than the corresponding values of M-CSF$_{WT}$ and M-CSF$_{C31S}$, and close to the theoretical R_g for the M-CSF monomer (Figure 3B, dashed line, $R_g = 17$ Å). To illustrate the oligomeric states of these three proteins in solution, low-resolution structures were reconstructed from the SAXS data (Figure 3D). The R_g values extracted from the SAXS profiles and the corresponding SAXS reconstructed structures support the premise that M-CSF$_{WT}$ and M-CSF$_{C31S}$ exist as dimers in solution, whereas M-CSF$_{C31S,M27R}$ is a monomer.

M-CSF$_{C31S,M27R}$ retains binding to the c-FMS receptor *in vitro*

Once we had verified that M-CSF$_{C31S,M27R}$ is a monomeric variant of M-CSF, we sought to test whether it could still bind the extracellular domains of c-FMS receptor (residues Met1–Glu512). Therefore, we measured the K_D of M-CSF$_{WT}$ and M-CSF$_{C31S,M27R}$ to the receptor using SPR spectroscopy. The different M-CSF proteins were attached to the chip, and binding to different concentrations of c-FMS in solution was measured (Figure 4). The K_D-binding constants between c-FMS and M-CSF$_{WT}$, M-CSF$_{C31S}$ (recently evaluated in [19]), and M-CSF$_{C31S,M27R}$ were 25.1 ± 7.50, 31.6 ± 1.11, and 61.5 ± 12.7 nM, respectively. We considered this small
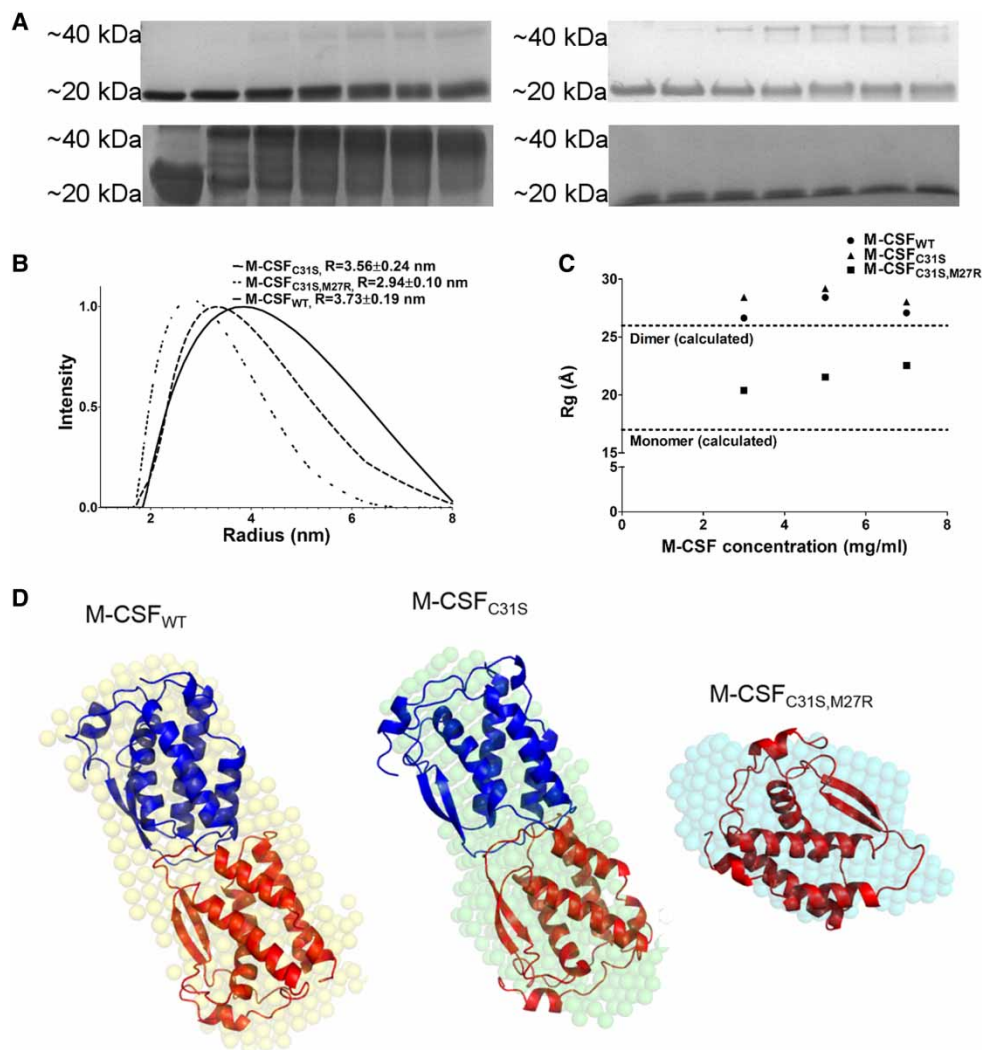
Figure 3. Biophysical assays to evaluate the oligomeric state of the M-CSF variants.

(**A**) For different M-CSF variants cross-linked with BS[3] reagent, the quantities of monomer (20 kDa) and dimer (40 kDa) were visualized on SDS–PAGE gel for human M-CSF (upper left), murine M-CSF (lower left), M-CSF$_{C31S}$ (upper right), and M-CSF$_{C31S,M27R}$ (lower right). (**B**) The distribution of hydration radii for M-CSF$_{WT}$ (solid line), M-CSF$_{C31S}$ (dashed line), and M-CSF$_{C31S,M27R}$ (dotted line) as measured by DLS. The calculated hydration radius is presented for each variant. (**C**) Radii of gyration determined by the in-house script for M-CSF$_{WT}$ and its two variants (M-CSF$_{C31S}$ and M-CSF$_{C31S,M27R}$). The dashed lines represent the theoretical R_g values for the M-CSF monomer (R_g = 17 Å) and M-CSF dimer (R_g = 26 Å) calculated from the crystal structure [PDB ID: 3UF2] using CRYSOL [36]. (**D**) SAXS structures of M-CSF$_{WT}$ and its two variants (M-CSF$_{C31S}$ and M-CSF$_{C31S,M27R}$). *Ab initio* models were reconstructed from SAXS data using the computer program GASBOR [37] and were averaged by the computer program DAMAVER [38]. The crystal structure of the M-CSF dimer (blue and red) and the structure of the monomer (extracted from the crystal structure of M-CSF, red) were aligned with the obtained SAXS models (yellow, M-CSF$_{WT}$; green, M-CSF$_{C31S}$; cyan, M-CSF$_{C31S,M27R}$) using PyMOL (http://www.pymol.org).

decrease in c-FMS affinity for M-CSF$_{C31S,M27R}$ as sufficiently minor to enable biological activity, and therefore proceeded to test the biological activity of M-CSF$_{C31S,M27R}$ in cell-based assays.

M-CSF$_{C31S,M27R}$ inhibits c-FMS phosphorylation

To determine whether M-CSF$_{C31S,M27R}$ binds and also antagonizes c-FMS, the phosphorylation of the receptor following incubation with different M-CSF variants was evaluated. First, murine BMMs were used, as murine c-FMS were previously shown to bind human M-CSF due to the high sequence identity between the two
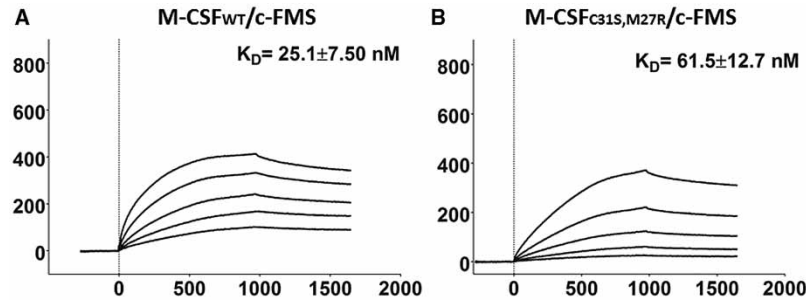
Figure 4. Affinity of M-CSF$_{WT}$ and M-CSF$_{C31S,M27R}$ to the c-FMS receptor, as detected by SPR.
Sensorgram of (**A**) M-CSF$_{WT}$ binding to c-FMS in concentrations up to 70 nM. (**B**) M-CSF$_{C31S,M27R}$ binding to c-FMS in concentrations up to 20 nM ($N = 3$). Values are means ± SD.

ligands [42,43]. BMMs were grown for 48 h in differentiation medium containing murine M-CSF$_{WT}$ (20 ng/ml) and RANKL (20 ng/ml). Then, the cells were starved and exposed to both murine M-CSF$_{WT}$ (0.5 nM) and either M-CSF$_{C31S}$ or M-CSF$_{C31S,M27R}$ (1 μM). The cells were lysed, and the expression and phosphorylation levels of c-FMS were evaluated using western blot. c-FMS phosphorylation level was quantified and normalized. Cells that were exposed to M-CSF$_{C31S}$ exhibited increased levels of phosphorylation compared with those that were exposed to M-CSF$_{WT}$, which served as the control. This finding indicates that the M-CSF$_{C31S}$ variant remains an agonist to the receptor (Figure 5A). In contrast, cells that were incubated with M-CSF$_{C31S,M27R}$ were found to have lower levels of phosphorylated c-FMS, i.e. M-CSF$_{C31S,M27R}$ acts as an antagonist to the receptor (Figure 5A).

Another experiment was conducted with human peripheral blood CD14$^+$ monocytes to determine whether M-CSF$_{C31S,M27R}$ has the same effect on human c-FMS. CD14$^+$ cells were grown in differentiation medium containing human M-CSF$_{WT}$ and murine RANKL for 72 h, and after starvation they were exposed to human M-CSF$_{WT}$ (0.5 nM) in combination with either M-CSF$_{C31S,M27R}$ or M-CSF$_{C31S}$ (100 nM). Again, the presence of M-CSF$_{C31S,M27R}$ resulted in decreased phosphorylation of c-FMS (Figure 5B), while M-CSF$_{C31S}$ acted as an agonist, inducing phosphorylation (Figure 5B). The effects of the different M-CSF variants on the phosphorylation of c-FMS may result from their dimerization tendency. While M-CSF$_{C31S}$ is a dimer and allows c-FMS dimerization and phosphorylation, the monomeric M-CSF$_{C31S,M27R}$ would probably not promote c-FMS dimerization, and therefore, its subsequent phosphorylation is reduced.

M-CSF$_{C31S,M27R}$ impairs differentiation of monocytes to osteoclasts

In light of the above-described decrease in phosphorylation, we hypothesized that incubation of M-CSF$_{C31S,M27R}$ with differentiating monocytes would result in decreased formation of osteoclasts. To test this premise, we incubated either BMMs or CD14$^+$ cells with murine or human M-CSF$_{WT}$ (20 ng/ml), respectively, and murine RANKL (20 ng/ml) together with M-CSF$_{C31S}$ and M-CSF$_{C31S,M27R}$ at concentrations of 50, 1000, and 5000 nM for BMMs and 50, 250, and 1000 nM for CD14$^+$ cells. The cells were allowed to differentiate for 96 h or until they reached full differentiation. In BMMs incubated with M-CSF$_{C31S}$, osteoclasts formed rapidly, and therefore, they differentiated only for 72 h. Then, the cells were stained with a TRAP staining kit (Figure 6A,B). We observed that in the presence of M-CSF$_{C31S}$, osteoclast formation was highly accelerated in the two lower concentrations and was significantly inhibited, in a dose-dependent manner, in the presence of M-CSF$_{C31S,M27R}$. The number of osteoclasts and the number of nuclei for each sample were quantified — exposure to M-CSF$_{C31S,M27R}$ led to a decrease in both parameters, in a dose-dependent manner, while M-CSF$_{C31S}$ produced the opposite result for 50 and 1000 nM concentrations (Figure 6A,B). Surprisingly, M-CSF$_{C31S}$ at a concentration of 5000 nM showed a reduction in both osteoclasts and nuclei number, suggesting that its agonistic activity occurs only at a certain concentration range. This inhibition of differentiation behavior was observed also for M-CSF$_{WT}$ [41]. These results are in agreement with the phosphorylation assay, i.e. the binding of M-CSF$_{C31S,M27R}$ to c-FMS prevented c-FMS dimerization and phosphorylation, which, in turn, prevented the differentiation of monocytes into osteoclasts.

To examine whether M-CSF$_{C31S}$ agonizes c-FMS in the same manner as human M-CSF$_{WT}$, we performed another BMMs differentiation assay in the presence of 50, 1000, and 5000 nM human M-CSF$_{WT}$ without the
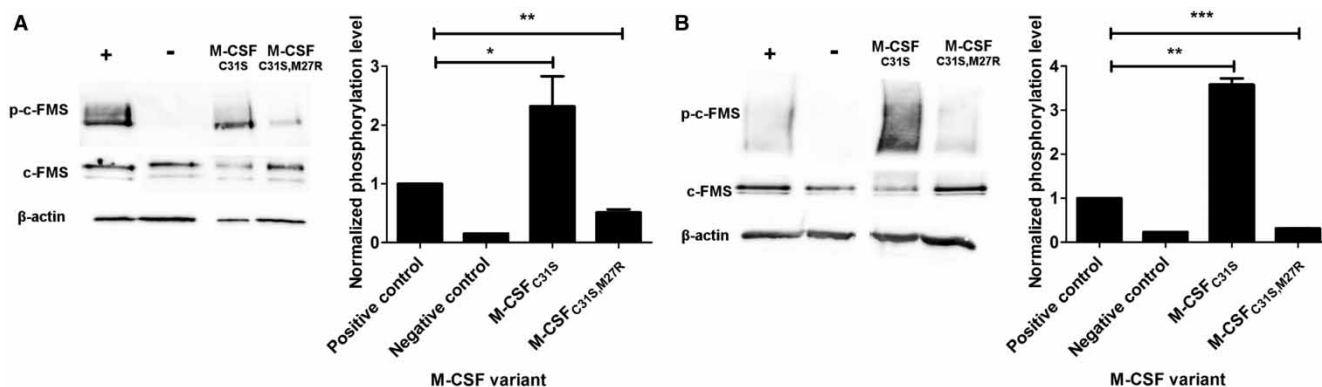
Figure 5. Evaluation of c-FMS phosphorylation in response to M-CSF variants.

(**A**) Phosphorylation of murine c-FMS on BMMs after incubation with 0.5 nM murine M-CSF (positive control, +), no M-CSF (negative control, −) or 0.5 nM murine M-CSF + 1 μM of M-CSF$_{C31S}$ or M-CSF$_{C31S,M27R}$. (**B**) Phosphorylation of human c-FMS on CD14$^+$ cells after incubation with 0.5 nM human M-CSF (positive control, +), no M-CSF (negative control, −) or 0.5 nM murine M-CSF + 100 nM of M-CSF$_{C31S}$ or M-CSF$_{C31S,M27R}$. All signals were normalized to those of β-actin, c-FMS expression, and the positive control in each experiment. Statistical analysis was calculated using the t-test, and each sample was compared with the positive control ($N = 3$). Values are means ± SEM. $^*P < 0.05$; $^{**}P < 0.01$; $^{***}P < 0.005$.

presence of murine M-CSF$_{WT}$. We have found that human M-CSF$_{WT}$, in this concentration range, inhibits both the numbers of osteoclasts and their nuclei, in a dose-dependent manner. Interestingly, in all the concentrations tested, human M-CSF$_{WT}$ was more active than M-CSF$_{C31S}$ in inhibiting cell differentiation, suggesting that the latter is a better c-FMS agonist (Supplementary Figure S3).

M-CSF$_{WT}$, M-CSF$_{C31S}$, and M-CSF$_{C31S,M27R}$ show different c-FMS activation/inhibition potencies

To elucidate the underlying mechanisms and dose–response nature of each M-CSF variant, a phosphorylation assay was performed using different concentrations of the M-CSF proteins. M-CSF$_{WT}$, M-CSF$_{C31S}$, and M-CSF$_{C31S,M27R}$ were incubated with BMMs for 1 min without murine M-CSF. The concentrations of M-CSF$_{WT}$ and M-CSF$_{C31S}$ (0.5–10 and 0.5–5000 nM, respectively) were chosen to allow bell-shaped curve activation, as seen for the differentiation assay. As expected, the bell-shaped curve occurred for M-CSF$_{WT}$ at lower concentrations than M-CSF$_{C31S}$ peaking at 5 and 10 nM, respectively. Interestingly, at the peak concentration, M-CSF$_{C31S}$ led to 10-fold increased phosphorylation compared with M-CSF$_{WT}$ and 40-fold compared with the positive control. In contrast, M-CSF$_{C31S,M27R}$ showed very limited c-FMS phosphorylation at any concentration other than 5 μM. At this concentration, it is likely that M-CSF$_{C31S,M27R}$ starts to dimerize, allowing c-FMS activation (Figure 7A).

Discussion

Intuitively, one would expect that c-FMS would be a prominent target for the development of antibody-based chemotherapeutics, but to date there is none that has been approved by the FDA. Similarly, to the best of our knowledge, there are only few reports of antibodies targeting M-CSF/c-FMS that have entered early-stage clinical trials [44]. An alternative — highly effective albeit challenging — strategy for creating non-immunoglobulin protein-based biological inhibitors lies in the engineering of natural ligand agonists to function as antagonists. Ligands differ from antibodies in that they naturally bind functionally important epitopes and thus provide a good jumping-off point for engineering protein–protein interactions.

A recent example from the Washington University School of Medicine showed how structural and functional information can be successfully applied to engineer a receptor antagonist from an activating ligand [8]. That study involved the development of an engineered form of the RANK ligand (RANKL) to function as a RANK receptor antagonist. It is known that RANKL binding to RANK initiates major signaling pathways, such as NFATc1, NF-κB, Akt/PKB, JNK, ERK, and p38, which are important for the differentiation, survival, and function of osteoclasts [45]. It is also known that the native ligand induces trimerization and activation of its
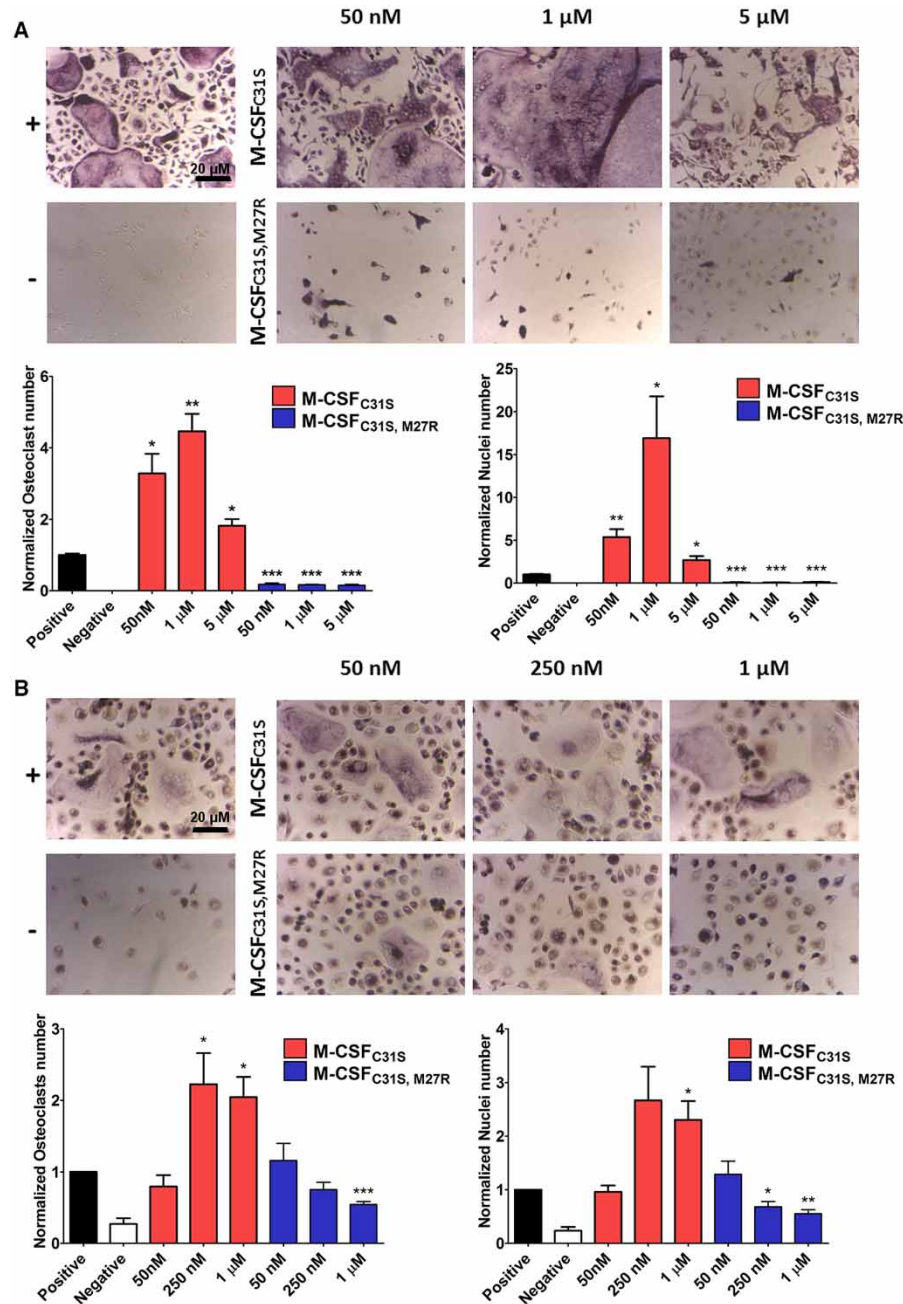
Figure 6. M-CSF$_{C31S,M27R}$ inhibits monocyte differentiation into osteoclasts.

(**A**) Differentiation of BMMs in the presence of murine M-CSF + RANKL (positive control), M-CSF without RANKL (negative control), and M-CSF + RANKL + M-CSF$_{C31S}$ or M-CSF$_{C31S,M27R}$ at concentrations of 50 nM and 1 μM was evaluated. Cells were stained using TRAP staining and photographed (upper panels). The number of osteoclasts (lower left) and number of nuclei in osteoclasts (lower right) were quantified. (**B**) Differentiation of CD14$^+$ in the presence of human M-CSF + murine RANKL (positive control), M-CSF without RANKL (negative control), and M-CSF + RANKL + M-CSF$_{C31S}$ or M-CSF$_{C31S,M27R}$ at concentrations of 50 nM, 250 nM, and 1 μM was evaluated. Cells were stained using TRAP and cells were photographed (upper panels). The number of osteoclasts (lower left) and number of nuclei in osteoclasts (lower right) were quantified. Statistical analysis was performed using the *t*-test, and each sample was compared with the positive control (*N* = 3). Values are means ± SEM. *$P < 0.05$; **$P < 0.01$; ***$P < 0.005$.
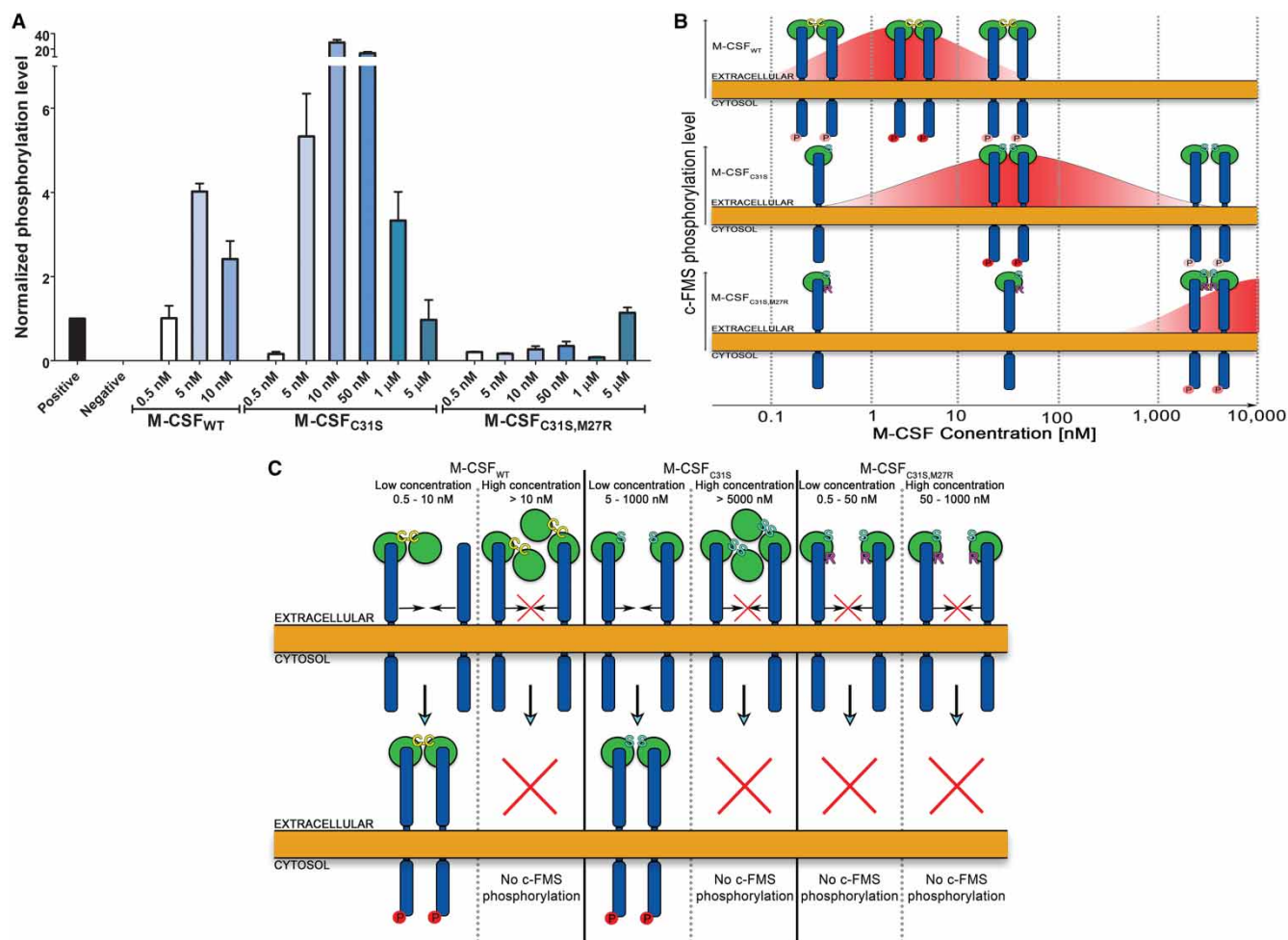
Figure 7. M-CSF variants activate c-FMS with different potencies.

(**A**) Quantification of phosphorylated murine c-FMS in the presence of 0.5 nM murine M-CSF (positive control), no M-CSF (negative control), M-CSF$_{WT}$ (0.5, 5, and 10 nM), M-CSF$_{C31S}$, and M-CSF$_{C31S,M27R}$ (0.5, 5, 10, 50, 1000, and 5000 nM) in the absence of murine M-CSF. All signals were normalized to those of β-actin, c-FMS expression, and the positive control in each experiment. Statistical analysis was calculated using the t-test, and each sample was compared with the positive control ($N = 3$). Values are means ± SEM. (**B**) An illustration showing c-FMS activation at different concentrations of M-CSF$_{WT}$, M-CSF$_{C31S}$, and M-CSF$_{C31S,M27R}$. (**C**) An illustration of the hypothesized inhibitory mechanism of M-CSF$_{WT}$, M-CSF$_{C31S}$, and M-CSF$_{C31S,M27R}$ at different oligomerization states as a function of their concentrations.

receptor through three distinct receptor-binding sites [46]. The Washington University group thus began their work by creating a single-chain trimer into which they introduced two generations of random mutations with the aim of abolishing one or two of the ligand's receptor-binding sites. The mutant ligand was then shown to bind to, but not activate, its receptor, thus acting as a receptor antagonist [8]. The promise of this approach was illustrated in a different study, showing that blocking RANK signaling inhibited osteoclastogenesis and reduced cancer cell migration, which could be exploited for the treatment of osteoporosis and cancer bone metastasis [47].

An attempt to convert M-CSF from dimer to monomer was undertaken some 20 years ago by the group of Rettenmier [24], when they engineered an M-CSF$_{C31S}$ mutant to prevent covalent disulfide bonds between opposing C31 residues in the dimer. There was, however, no considerable attempt to understand the biological effect of this mutant, M-CSF$_{C31S}$, on the M-CSF/c-FMS signal transduction cascade in relevant mammalian cells. Furthermore, the antagonistic activity of M-CSF$_{C31S}$ in the presence of the wild-type M-CSF agonist was not tested. In our recent study, we used SPR to show that M-CSF$_{C31S}$ does not exhibit dimerization in concentrations up to 500 nM [19], which may potentially lead to an antagonistic effect. Curiously, we show here that

the addition of M-CSF$_{C31S}$ mutant in higher concentrations, together with M-CSF$_{WT}$ to BMMs or human CD14$^+$ cells, results in further enhancement of M-CSF-mediated c-FMS phosphorylation (Figure 5) and osteoclast differentiation (Figure 6). These results limit the therapeutic potential of the M-CSF$_{C31S}$ molecule. We reasoned that the lack of antagonistic activity of M-CSF$_{C31S}$ was due to the fact that even though the intermolecular disulfide interactions had been abolished in M-CSF$_{C31S}$, the remaining non-covalent interactions facilitate M-CSF homodimerization in the micro-molar concentration range (Figures 1 and 3) and, hence, the subsequent activation of the M-CSF/c-FMS signal transduction cascade.

Our strategy to engineer a monomeric M-CSF variant for improved antagonism to c-FMS rested on combining the C31S and M27R mutations, which block covalent and non-covalent interactions, respectively, between the two M-CSF monomers. The M27 residue was identified as contributing substantially to the non-covalent dimer interactions based on the solved structure of M-CSF$_{C31S}$ and our energy calculations (Figures 1 and 2). Importantly, M27 does not contribute to interactions with the c-FMS receptor. Moreover, because M27 extends deep into the opposing M-CSF monomer while having essentially no intramolecular interactions, the M27R mutation abolishes dimer formation without affecting monomer stability.

The prevention of monomer self-association was observed in SAXS measurements of soluble M-CSF$_{C31S, M27R}$ but not of M-CSF$_{C31S}$ or M-CSF$_{WT}$ (Figure 3). SAXS measurements were performed to obtain low-resolution structures of M-CSF$_{WT}$ and its two variants (M-CSF$_{C31S}$ and M-CSF$_{C31S,M27R}$) in solution. With these experiments, we demonstrated that M-CSF$_{WT}$ and M-CSF$_{C31S}$ have similar sizes and shapes, whereas M-CSF$_{C31S,M27R}$ is smaller and compatible with a monomeric structure of M-CSF. On the other hand, the mutations in the monomeric M-CSF$_{C31S,M27R}$ appear to slightly decrease its affinity for c-FMS relative to M-CSF$_{C31S}$ and M-CSF$_{WT}$, presumably as a result of decreased avidity, due to its inability to bind to two c-FMS molecules (Figure 4).

To test whether the M-CSF variants can inhibit M-CSF-mediated activities in cells, we explored their effects on early signaling events, namely, c-FMS phosphorylation and differentiation of osteoclasts. Not surprisingly, M-CSF$_{C31S,M27R}$ significantly reduced c-FMS phosphorylation and cell differentiation of BMMs and human CD14$^+$ cells, whereas M-CSF$_{C31S}$ induced these processes. The differences, observed in the phosphorylation and differentiation assays between these two cell types, are likely caused due to the origins of different species and because the BMMs were taken directly from the bone marrow, while CD14$^+$ cells were taken from peripheral blood and therefore the population might be less homogeneous in terms of monocyte subpopulations.

To shed light on the agonistic/antagonistic properties of each of the M-CSF variants, we have conducted a phosphorylation experiment using a broad range of concentrations of these proteins. The range of concentrations we used was selected to allow the formation of a bell-shaped curve typical for M-CSF/c-FMS activation and inhibition. As expected, M-CSF$_{WT}$ and M-CSF$_{C31S}$ showed a similar curve in different protein concentrations with M-CSF$_{WT}$ phosphorylating c-FMS at lower concentrations. Unexpectedly, M-CSF$_{C31S}$ prompted much higher phosphorylation levels than M-CSF$_{WT}$, with a 10-fold increase in phosphorylated c-FMS at 10 nM. M-CSF$_{C31S,M27R}$ did not exhibit phosphorylation capabilities in concentrations lower than 5 μM (Figure 7A,B).

With this in mind, we hypothesized that the mechanism causing this c-FMS activation curve is based on the combination of M-CSF ligand dimerization tendencies and c-FMS molecules that are occupied by the ligand. Therefore, we suggest a model for c-FMS activation by these different variants (Figure 7C). For example, we assume that in the case of M-CSF$_{WT}$ at concentrations higher than 5 nM, many c-FMS molecules are bound to a covalently dimeric ligand preventing two c-FMS receptors from coming in close proximity, therefore abolishing dimerization and phosphorylation of the receptor. On the other hand, in the case of M-CSF$_{C31S}$ in the same concentration, c-FMS molecules are bound to a monomeric M-CSF$_{C31S}$, thus increasing the local concentration and the driving force for M-CSF dimerization and c-FMS phosphorylation. In the presence of high M-CSF$_{C31S}$ concentrations, it becomes a non-covalent dimer, thus leading to the same effect as high M-CSF$_{WT}$ concentrations.

Our study allows better understanding of M-CSF–M-CSF interactions and their influence on M-CSF/c-FMS function. The application of these insights led to the rational engineering of an M-CSF mutant that exhibits promise for further development as a therapeutic. We, thus, have at our disposal new tools for studying the molecular mechanisms and cell signaling pathways that are related to M-CSF/c-FMS ligand/receptor interactions and, perhaps more importantly, similar biological processes as well. The broader implications of the study are that it provides support for the approach that rational engineering of ligands and/or their receptors could be the way forward to complement antibody-based approaches for developing the next generation of

PORTLAND
PRESS

therapeutics, including, but not limited to, targeted drug-delivery agents and selective tissue-targeting probes. In particular, our strategy for converting a ligand agonist into an antagonist can be applied to other ligand/ RTK pairs. The game plan for developing protein variants that is presented here will thus find utility in providing significant insights into the principles of molecular recognition and protein structure–function relationships in addition to its potential applicability for the development of therapeutics.

Abbreviations

BMMs, bone marrow-derived monocytes; BS³, bis(sulfosuccinimidyl)suberate; DLS, dynamic light scattering; EDC, 1-ethyl-3-(3-dimethylaminopropyl)-carbodiimide; ESRF, European Synchrotron Radiation Facility; FBS, fetal bovine serum; FDPB, finite difference Poisson–Boltzmann; HRP, horseradish peroxidase; LPS, lipopolysaccharide; M-CSF, macrophage colony-stimulating factor; α-MEM, minimun essential medium eagle (alpha modified); PBST, phosphate-buffered saline + 0.005% Tween; RANKL, receptor activator of nuclear factor κ B ligand; RMSD, root-mean-square deviation; RTK, receptor tyrosine kinase; SAXS, small-angle X-ray scattering; SPR, surface plasmon resonance; sulfo-NHS, N-hydroxysuccinimide; TRAP, tartrate-resistant acid phosphatase; WT, wild type.

Author Contribution

Y.Z., L.R., A.B., M.K., N.L., and N.P. designed research; Y.Z., L.R., A.B., H.H., S.I., and A.S. performed research; Y.Z., L.R., A.B., S.I., A.S., B.A., M.K., N.L., and N.P. analyzed data; Y.Z., L.R., M.K., N.L., and N.P. wrote the paper. All authors edited the manuscript and approved the final version.

Competing Interests

The Authors declare that there are no competing interests associated with the manuscript.

References

1   Kim, K.-T., Choi, H.-H., Steinmetz, M.O., Maco, B., Kammerer, R.A., Ahn, S.Y. et al. (2005) Oligomerization and multimerization are critical for angiopoietin-1 to bind and phosphorylate Tie2. *J. Biol. Chem.* **280**, 20126–20131 doi:10.1074/jbc.M500292200
2   Jones, D.J., Silverman, A.P. and Cochran, J.R. (2008) Developing therapeutic proteins by engineering ligand-receptor interactions. *Trends Biotechnol.* **26**, 498–505 doi:10.1016/j.tibtech.2008.05.009
3   Spiess, K., Jeppesen, M.G., Malmgaard-Clausen, M., Krzywkowski, K., Dulal, K., Cheng, T. et al. (2015) Rationally designed chemokine-based toxin targeting the viral G protein-coupled receptor US28 potently inhibits cytomegalovirus infection *in vivo. Proc. Natl Acad. Sci. U.S.A.* **112**, 8427–8432 doi:10.1073/pnas.1509392112
4   Boesen, T.P., Soni, B., Schwartz, T.W. and Halkier, T. (2002) Single-chain vascular endothelial growth factor variant with antagonist activity. *J. Biol. Chem.* **277**, 40335–40341 doi:10.1074/jbc.M204107200
5   Fuh, G., Cunningham, B.C., Fukunaga, R., Nagata, S., Goeddel, D.V. and Wells, J.A. (1992) Rational design of potent antagonists to the human growth hormone receptor. *Science* **256**, 1677–1680 doi:10.1126/science.256.5064.1677
6   Hsu, Y.-R., Wu, G.-M., Mendiaz, E.A., Syed, R., Wypych, J., Toso, R. et al. (1997) The majority of stem cell factor exists as monomer under physiological conditions: implications for dimerization mediating biological activity. *J. Biol. Chem.* **272**, 6406–6415 doi:10.1074/jbc.272.10.6406
7   Papo, N., Silverman, A.P., Lahti, J.L. and Cochran, J.R. (2011) Antagonistic VEGF variants engineered to simultaneously bind to and inhibit VEGFR2 and αvβ3 integrin. *Proc. Natl Acad. Sci. U.S.A.* **108**, 14067–14072 doi:10.1073/pnas.1016635108
8   Warren, J.T., Nelson, C.A., Decker, C.E., Zou, W., Fremont, D.H. and Teitelbaum S. L. (2014) Manipulation of receptor oligomerization as a strategy to inhibit signaling by TNF superfamily members. *Sci. Signal.* **7**, ra80 doi:10.1126/scisignal.2004948

9   Tushinski, R.J., Oliver, I.T., Guilbert, L.J., Tynan, P.W., Warner, J.R. and Stanley, E.R. (1982) Survival of mononuclear phagocytes depends on a lineage-specific growth factor that the differentiated cells selectively destroy. *Cell* **28**, 71–81 doi:10.1016/0092-8674(82)90376-2

10   Yasuda, H., Shima, N., Nakagawa, N., Yamaguchi, K., Kinosaki, M., Mochizuki, S.-i. et al. (1998) Osteoclast differentiation factor is a ligand for osteoprotegerin/osteoclastogenesis-inhibitory factor and is identical to TRANCE/RANKL. *Proc. Natl Acad. Sci. U.S.A.* **95**, 3597–3602 doi:10.1073/pnas.95.7.3597

11   Jeffery, J.J., Lux, K., Vogel, J.S., Herrera, W.D., Greco, S., Woo, H.-H. et al. (2014) Autocrine inhibition of the c-fms proto-oncogene reduces breast cancer bone metastasis assessed with *in vivo* dual-modality imaging. *Exp. Biol. Med.* **239**, 404–413 doi:10.1177/1535370214522588

12   Sousa, S. and Määttä, J. (2016) The role of tumour-associated macrophages in bone metastasis. *J. Bone Oncol.* **5**, 135–138 doi:10.1016/j.jbo.2016.03.004

13   Hung, J.Y., Horn, D., Woodruff, K., Prihoda, T., LeSaux, C., Peters, J. et al. (2014) Colony-stimulating factor 1 potentiates lung cancer bone metastasis. *Lab. Invest.* **94**, 371–381 doi:10.1038/labinvest.2014.1

14   Aharinejad, S., Abraham, D., Paulus, P., Abri, H., Hofmann, M., Grossschmidt, K. et al. (2002) Colony-stimulating factor-1 antisense treatment suppresses growth of human tumor xenografts in mice. *Cancer Res.* **62**, 5317–5324 PMID:12235002

15   Menke, J., Kriegsmann, J., Schimanski, C.C., Schwartz, M.M., Schwarting, A. and Kelley, V.R. (2012) Autocrine CSF-1 and CSF-1 receptor coexpression promotes renal cell carcinoma growth. *Cancer Res.* **72**, 187–200 doi:10.1158/0008-5472.CAN-11-1232

16   Patsialou, A., Wyckoff, J., Wang, Y., Goswami, S., Stanley, E.R. and Condeelis, J.S. (2009) Invasion of human breast cancer cells *in vivo* requires both paracrine and autocrine loops involving the colony-stimulating factor-1 receptor. *Cancer Res.* **69**, 9498–9506 doi:10.1158/0008-5472.CAN-09-1868

17   Ide, H., Seligson, D.B., Memarzadeh, S., Xin, L., Horvath, S., Dubey, P. et al. (2002) Expression of colony-stimulating factor 1 receptor during prostate development and prostate cancer progression. *Proc. Natl Acad. Sci. U.S.A.* **99**, 14404–14409 doi:10.1073/pnas.222537099

18   Pandit, J., Bohm, A., Jancarik, J., Halenbeck, R., Koths, K. and Kim, S. (1992) Three-dimensional structure of dimeric human recombinant macrophage colony-stimulating factor. *Science* **258**, 1358–1362 doi:10.1126/science.1455231

19   Rosenfeld, L., Shirian, J., Zur, Y., Levaot, N., Shifman, J.M. and Papo, N. (2015) Combinatorial and computational approaches to identify interactions of macrophage colony-stimulating factor (M-CSF) and its receptor c-FMS. *J. Biol. Chem.* **290**, 26180–26193 doi:10.1074/jbc.M115.671271

20   Felix, J., De Munck, S., Verstraete, K., Meuris, L., Callewaert, N., Elegheert, J. et al. (2015) Structure and assembly mechanism of the signaling complex mediated by human CSF-1. *Structure* **23**, 1621–1631 doi:10.1016/j.str.2015.06.019

21   Douglass, T.G., Driggers, L., Zhang, J.G., Hoa, N., Delgado, C., Williams, C.C. et al. (2008) Macrophage colony stimulating factor: not just for macrophages anymore! A gateway into complex biologies. *Int. Immunopharmacol.* **8**, 1354–1376 doi:10.1016/j.intimp.2008.04.016

22   Pixley, F.J. and Stanley, E.R. (2004) CSF-1 regulation of the wandering macrophage: complexity in action. *Trends Cell Biol.* **14**, 628–638 doi:10.1016/j.tcb.2004.09.016

23   Ross, F.P. (2006) M-CSF, c-Fms, and signaling in osteoclasts and their precursors. *Ann. N. Y. Acad. Sci.* **1068**, 110–116 doi:10.1196/annals.1346.014

24   Deng, P., Wang, Y.-L., Pattengale, P.K. and Rettenmier, C.W. (1996) The role of individual cysteine residues in the processing, structure, and function of human macrophage colony-stimulating factor. *Biochem. Biophys. Res. Commun.* **228**, 557–566 doi:10.1006/bbrc.1996.1698

25   Otwinowski, Z. and Minor, W. (1997) Processing of X-ray diffraction data collected in oscillation mode. *Methods Enzymol.* **276**, 307–326 doi:10.1016/S0076-6879(97)76066-X

26   McCoy, A.J., Grosse-Kunstleve, R.W., Adams, P.D., Winn, M.D., Storoni, L.C. and Read, R.J. (2007) *Phaser* crystallographic software. *J. Appl. Crystallogr.* **40**, 658–674 doi:10.1107/S0021889807021206

27   Winn, M.D., Ballard, C.C., Cowtan, K.D., Dodson, E.J., Emsley, P., Evans, P.R. et al. (2011) Overview of the *CCP*4 suite and current developments. *Acta Crystallogr. Sect. D* **67**, 235–242 doi:10.1107/S0907444910045749

28   Emsley, P. and Cowtan, K. (2004) *Coot*: model-building tools for molecular graphics. *Acta Crystallogr. Sect. D Biol. Crystallogr.* **60**, 2126–2132 doi:10.1107/S0907444904019158

29   Adams, P.D., Afonine, P.V., Bunkóczi, G., Chen, V.B., Davis, I.W., Echols, N. et al. (2010) *PHENIX*: a comprehensive Python-based system for macromolecular structure solution. *Acta Crystallogr. Sect. D Biol. Crystallogr.* **66**, 213–221 doi:10.1107/S0907444909052925

30   Kosloff, M., Travis, A.M., Bosch, D.E., Siderovski, D.P. and Arshavsky, V.Y. (2011) Integrating energy calculations with functional assays to decipher the specificity of G protein–RGS protein interactions. *Nat. Struct. Mol. Biol.* **18**, 846–853 doi:10.1038/nsmb.2068

31   Sridharan, S., Nicholls, A., Honig, B., Nicholls, A. and Honig, B. (1992) A new vertex algorithm to calculate solvent accessible surface-areas. *FASEB J.* **6**, A174

32   Sheinerman, F.B., Al-Lazikani, B. and Honig, B. (2003) Sequence, structure and energetic determinants of phosphopeptide selectivity of SH2 domains. *J. Mol. Biol.* **334**, 823–841 doi:10.1016/j.jmb.2003.09.075

33   Konarev, P.V., Volkov, V.V., Sokolova, A.V., Koch, M.H.J. and Svergun, D.I. (2003) *PRIMUS*: a windows PC-based system for small-angle scattering data analysis. *J. Appl. Crystallogr.* **36**, 1277–1282 doi:10.1107/S0021889803012779

34   Akabayov, B., Akabayov, S.R., Lee, S.-J., Tabor, S., Kulczyk, A.W. and Richardson, C.C. (2010) Conformational dynamics of bacteriophage T7 DNA polymerase and its processivity factor, *Escherichia coli* thioredoxin. *Proc. Natl Acad. Sci. U.S.A.* **107**, 15033–15038 doi:10.1073/pnas.1010141107

35   Svergun, D.I. (1992) Determination of the regularization parameter in indirect-transform methods using perceptual criteria. *J. Appl. Crystallogr.* **25**, 495–503 doi:10.1107/S0021889892001663

36   Barberato, C., Barberato, C. and Koch, M.H.J. (1995) CRYSOL — a program to evaluate X-ray solution scattering of biological macromolecules from atomic coordinates. *J. Appl. Crystallogr.* **28**, 768–773 doi:10.1107/S0021889895007047

37   Svergun, D.I., Petoukhov, M.V. and Koch, M.H.J. (2001) Determination of domain structure of proteins from X-ray solution scattering. *Biophys. J.* **80**, 2946–2953 doi:10.1016/S0006-3495(01)76260-1

38   Volkov, V.V. and Svergun, D.I. (2003) Uniqueness of *ab initio* shape determination in small-angle scattering. *J. Appl. Crystallogr.* **36**, 860–864 doi:10.1107/S0021889803000268

39   Levaot, N., Simoncic, P.D., Dimitriou, I.D., Scotter, A., La Rose, J., Ng, A.H.M. et al. (2011) 3BP2-deficient mice are osteoporotic with impaired osteoblast and osteoclast functions. *J. Clin. Invest.* **121**, 3244–3257 doi:10.1172/JCI45843

40   Abràmoff, M.D., Magalhães, P.J. and Ram, S. J. (2004) Image processing with imageJ. *Biophotonics Int.* **11**, 36–41

41   Chen, X., Liu, H., Focia, P.J., Shim, A.H.-R. and He, X. (2008) Structure of macrophage colony stimulating factor bound to FMS: diverse signaling assemblies of class III receptor tyrosine kinases. *Proc. Natl Acad. Sci. U.S.A.* **105**, 18267–18272 doi:10.1073/pnas.0807762105

42   DeLamarter, J.F., Hession, C., Semon, D., Gough, N.M., Rothenbuhler, R. and Mernod, J.-J. (1987) Nucleotide sequence of a cDNA encoding murine CSF-1 (macrophage-CSF). *Nucleic Acids Res.* **15**, 2389–2390 doi:10.1093/nar/15.5.2389

43   Elegheert, J., Desfosses, A., Shkumatov, A.V., Wu, X., Bracke, N., Verstraete, K. et al. (2011) Extracellular complexes of the hematopoietic human and mouse CSF-1 receptor are driven by common assembly principles. *Structure* **19**, 1762–1772 doi:10.1016/j.str.2011.10.012

44   Hamilton, J.A., Cook, A.D. and Tak, P.P. (2017) Anti-colony-stimulating factor therapies for inflammatory and autoimmune diseases. *Nature* **16**, 53–70 doi:10.1038/nrd.2016.231

45   Feng, X. (2005) RANKing intracellular signaling in osteoclasts. *IUBMB Life* **57**, 389–395 doi:10.1080/15216540500137669

46   Nelson, C.A., Warren, J.T., Wang, M.W.-H., Teitelbaum, S.L. and Fremont, D.H.. (2012) RANKL employs distinct binding modes to engage RANK and the osteoprotegerin decoy receptor. *Structure* **20**, 1971–1982 doi:10.1016/j.str.2012.08.030

47   Shin, M., Matsuo, K., Tada, T., Fukushima, H., Furuta, H., Ozeki, S. et al. (2011) The inhibition of RANKL/RANK signaling by osteoprotegerin suppresses bone invasion by oral squamous cell carcinoma cells. *Carcinogenesis* **32**, 1634–1640 doi:10.1093/carcin/bgr198

TABLE S1: Crystallographic and refinement statistics for the M-CSF$_{C31S}$ Structure

Data collection	
X-ray source	ESRF BM14
Wavelength (Å)	0.979
D_{min}(Å)	39.66-2.0 (2.07-2.0)
Space group	P212121
Cell dimensions	
a,b,c (Å)	33.27, 65.47,158.63
α,β,γ (°)	90.0,90.0,90.0
Total reflections	671,737
Unique reflections	20,774
Rpim (%)	2.5(50.8)
Completeness (%)	95.1 (85.7)
I/σI	26.5 (1.2)
Redundancy	8.7(8.2)
$CC_{1/2}$	(72.7)
Refinement	
Refinement resolution (Å)	39.66-2.0
Total reflections used	20,773
RMSD bond lengths (Å)	0.008
RMSD bond angles (°)	1.01
Ramachandran plot	
Favored (%)	98
Outliers (%)	0.00
R_{work}/R_{free} (%)	20.12/26.00
Protein atoms	2437
Solvent molecules	2569
Average B-factor (Å^2)	37.84
Protein	38.08
Solvent	33.46
Wilson B factor (Å^2)	25.56
PDB ID	**5LXF**

Values in parentheses correspond to the highest resolution shell of the data.

FIGURE S1: Per-residue energy contributions to interaction across the M-CSF dimer interface, calculated as described in Methods. np = non-polar, sc = side-chain, all = full-residue.
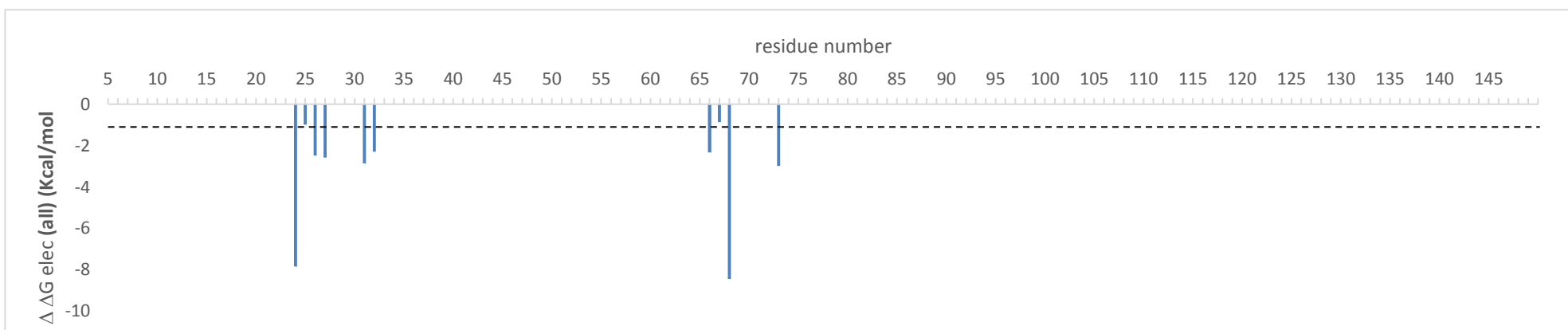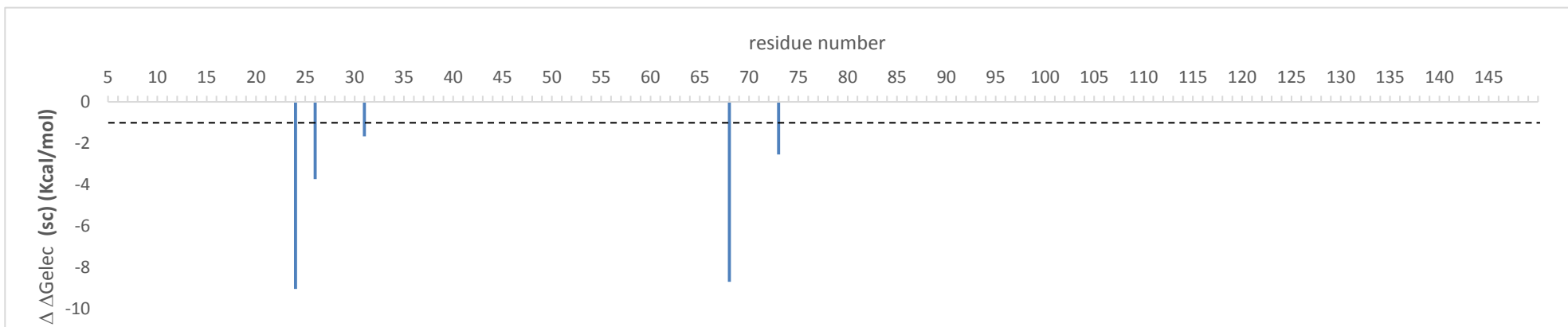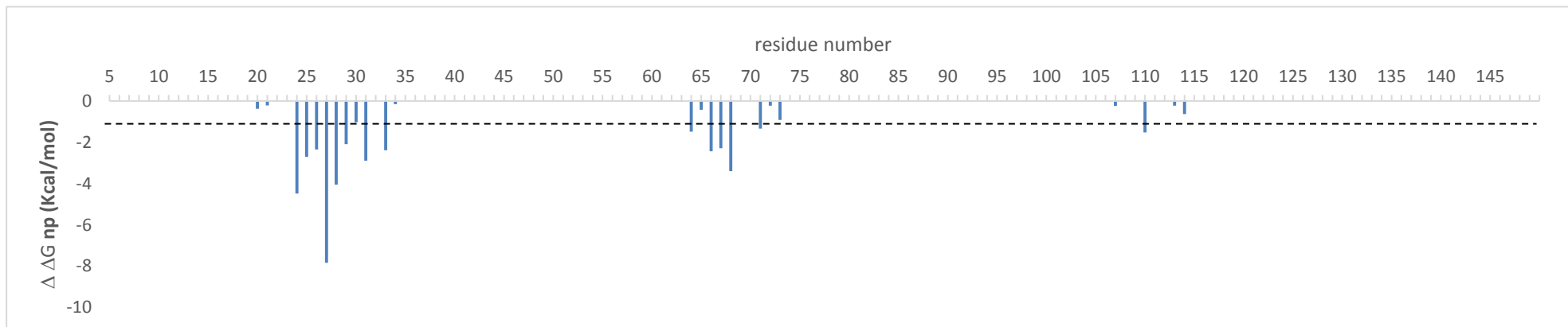
TABLE S2: Overall parameters for X-ray scattering of M-CSF$_{WT}$, M-CSF$_{C31S}$, and M-CSF$_{C31S,M27R}$

Species	Method	Rg (Å)		
		3 mg/mL	5 mg/mL	7 mg/mL
M-CSF monomer	CRYSOL[¶]	17		
M-CSF dimer	CRYSOL	26		
M-CSF$_{WT}$	Guinier[§]	27.7	30.1	27.3
M-CSF$_{WT}$	Script*	26.65	28.42	27.09
M-CSF$_{C31S}$	Guinier	29	26.6	26.9
M-CSF$_{C31S}$	Script	28.44	29.19	28.04
M-CSF$_{C31S,M27R}$	Guinier	20.3	23.3	24
M-CSF$_{C31S,M27R}$	Script	20.4	21.56	22.56

R$_g$, radius of gyration

[¶]Determined using the software CRYSOL (1) and the crystal structure of M-CSF [PDB ID code 3UF2]. The coordinates of the monomer were extracted from the crystal structure in PyMOL (http://www.pymol.org)

[§]Determined by linear fitting to the Guinier region

*Determined by in-house script (2) that performs a coarse automatic search for the best fitting parameters using GNOM (3).
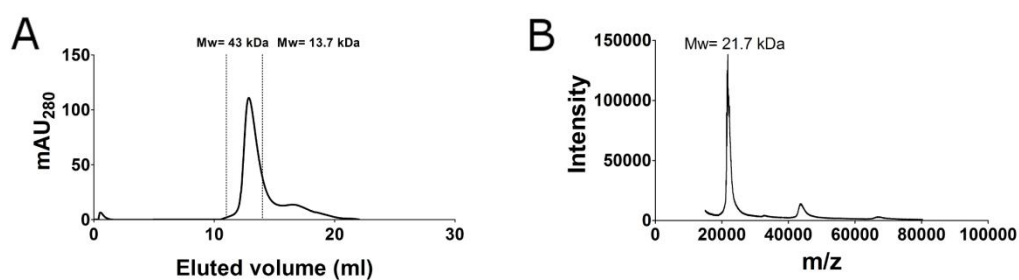

FIGURE S2: Purification of M-CSF$_{C31S,M27R}$.
M-CSF$_{C31S,M27R}$ was purified following production in *P. pastoris* yeast. (A) SEC chromatogram using Superdex 75 10/300. (B) Mass spectrometry analysis of the purified protein.
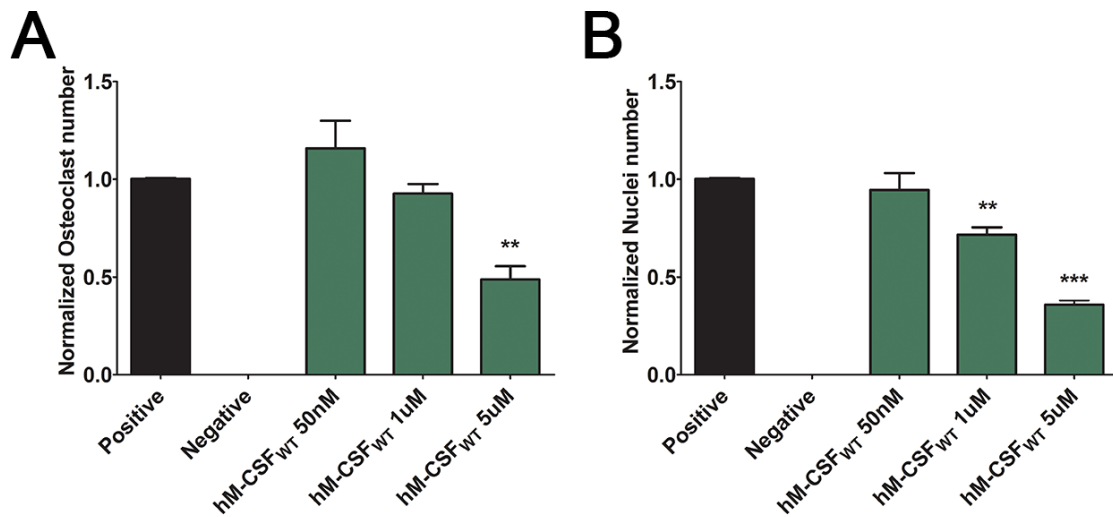
FIGURE S3: Osteoclasts differentiation in the presence of human M-CSF_WT
Murine BMMs were seeded for differentiation in the presence of murine M-CSF + RANKL (positive control), M-CSF without RANKL (negative control), and M-CSF + RANKL + human M-CSF$_{WT}$ at concentrations of 50 nM, 1 μM and 5 μM was evaluated. The number of osteoclasts (A) and number of nuclei in osteoclasts (B) were quantified. Statistical analysis was performed using a t-test, each sample was compared to the positive control. N = 3. Values are means ± SEM. *, $p<0.05$; **, $p<0.01$; ***, $p<0.005$.

REFERENCES

1. Barberato C, Koch MHJ, Molecular E, Outstation H (1995) CRYSOL - a Program to Evaluate X-ray Solution Scattering of Biological Macromolecules from Atomic Coordinates. *J Appl Crystallogr* 28(6):768–773.
2. Akabayov B, et al. (2010) Conformational dynamics of bacteriophage T7 DNA polymerase and its processivity factor, Escherichia coli thioredoxin. *Proc Natl Acad Sci* 107 (34):15033–15038.
3. Svergun DI (1992) Determination of the regularization parameter in indirect-transform methods using perceptual criteria. *J Appl Crystallogr* 25(4):495–503.